Supplementary materials for

Rational heterostructure stacking enables 23% wide-bandgap perovskite solar cells by side-reaction inhibition

Tianyu Huang *et al.*

Experimental Section

Materials:

Lead dibromide ($PbBr_2$, 99%), lead diiodide (PbI_2, 99%), [2-(3,6-Dimethoxy-9H-carbazol-9-yl)ethyl]phosphonic Acid (MeO-2PACz) and [2-(9H-Carbazol-9-yl)ethyl] phosphonic Acid (2PACz) were purchased from Tokyo Chemical Industry Co., Ltd (TCI, Japan). Bathocuproine (BCP), ethane-1,2-diamine dihydrobromide ($EDABr_2$, >99%), and were purchased from Xi'an Polymer Light Technology Corp (China). Formamidinium iodide (FAI, >99.99%) and methylammonium iodide (MAI, >99.99%) were purchased from Greatcell Solar. Methylammonium bromide (MABr, >99.99%) and Fullerene C60 (C60, >99.9%) were purchased from Advanced Election Technology Co., Ltd (China). Cesium iodide (CsI, 99.999%) was purchased from Sigma–Aldrich (USA). [6,6]-Phenyl-C61-butyric acid methyl ester (PCBM) was purchased from Nano-C Tech. (USA). 2-propanol-d8 (>99.9%) was purchased from konoscience (China). Silver (Ag) was purchased from a commercial source with high purity. Isopropanol (IPA), ethanol, methanol, chlorobenzene (CB), anisole, ultra-dry dimethylformamide (DMF), and ultra-dry dimethyl sulfoxide (DMSO) were purchased from commercial sources (Acros). All reagents were used as received without further purification.

Device preparation:

Small and 1-cm^2 active area perovskite solar cell: The PSC devices studied were fabricated on an FTO glass substrate (purchased from Advanced Election Technology Co., Ltd (China). FTO glasses were cleaned through sequential ultrasonication in soap water, deionized H_2O, acetone, and IPA for 20 min each followed by 15 min of UV-Ozone treatment. The following operations were all carried out in an N_2-filled glovebox with H_2O and O_2 concentrations of <0.1 ppm (at room temperature). For the fabrication of PSCs, MeO-2PACz/2PACz = 3/1(m/m) powder was dissolved in anhydrous ethanol at 0.3-0.5 mg/ml and then dispersed ultrasonically for 15 min (at 30-40℃) before use, called self-assembly monolayer (SAM) in the following part. 100 L of SAM solution was added onto the pre-cleaned FTO substrates and rested for 10 s, and then spin-coated at 4,000 rpm for 30 s and annealed at 100℃ for 8-10 min. After heating, the FTO/SAM substrates were washed dynamically during the same spin-coating program by dripping 100 μL of ethanol or IPA 2 times onto them. Perovskite precursor solution ($Cs_{0.05}MA_{0.15}FA_{0.8}PbI_{2.25}Br_{0.75}$) was prepared by dissolving the PbI_2, $PbBr_2$, MABr, CsI, and

FAI in a mixed solvent (4:1 in volume) of DMF and DMSO with a concentration of 1.5 M. Without filtering and dilution, the perovskite precursor solution was spin-coated on the SAM-coated FTO substrate following an improved processing program: 2000 rpm for 10 s with a ramping rate of 500 rpm s^{-1}, and 6000 rpm for 30 s with a ramping rate of 1000 rpm s^{-1}. 200 μL anisole was poured on the spinning substrate at the 25th second during the consecutive two-step spin-coating program (the temperature of the glove box is around 23°C). The perovskite film was subsequently annealed at 100°C for 20 min. Then, the as-prepared perovskite films were treated with a solution composed of 0.5 mg of $EDABr_2$, 0.5 mg of MAI, 5 μL of DMF, and 1 mL of IPA/Methanol=7/1 (v/v). The treatment was carried by depositing the mixed solution (50 μL) onto the perovskite film surface when spun at a rate of 4000 rpm. The film was then annealed at 100°C for 10 min. Further, the PCBM solution (20 mg mL^{-1} in CB) was spin-coated on the perovskite layer at 1,000 rpm for 30 s (with a ramping rate of 200 rpm s^{-1}). After that, BCP (1 mg mL^{-1} in ethanol) was spin-coated at 5,000 rpm with a ramping rate of 2,000 rpm s^{-1} for 30 s. A 120-nm thick Ag electrode was thermally evaporated onto the samples in the vacuum chamber ($<4\times10^{-4}$ Pa) with a deposition rate of 1.0-1.2 Å s^{-1}.

Minimodules: the 5 cm×5 cm patterned FTO glass was washed as reported. The following operations were all carried out in an N_2-filled glovebox with H_2O and O_2 concentrations of <0.1 ppm (at room temperature). The SAM solution was spin-coated onto the patterned FTO substrates as reported previously. Subsequently, the perovskite precursor solution (a concentration of 1.4M $Cs_{0.05}MA_{0.15}FA_{0.8}PbI_{2.25}Br_{0.75}$ in DMSO/DMF=1/4 volume ratio) was blade-coated onto the HTM-covered FTO glass substrates with a gap of 30 μm and a movement speed of 15 mm s^{-1} followed by a thermal annealing process at 100°C for 15 min. Then, the as-prepared perovskite films were treated with solution composed of 0.5 mg of $EDABr_2$, 0.5 mg of MAI, 5 μL of DMF, and 1 mL of IPA/methanol=7/1 (volume ratio). The treatment was carried by depositing the mixed solution (100 μL) onto the perovskite film surface when spun at a rate of 4000 rpm. The film was then annealed at 100°C for 10 min. Then, C60 was thermally evaporated onto the perovskite film (20 nm, 0.3 Å s^{-1}). 20 nm of SnO_2 were then deposited by thermal atomic layer deposition (ALD). Tetrakis(dimethylamino)tin(IV) (TDMASn) was used as the Sn precursor and was held at 60°C in a stainless-steel container. Water was used as oxidant, and was delivered from a stainless-steel container without active heating, whereas the precursor delivery manifold was heated to 115°C, 140 cycles lead to 20 nm SnO_2. Then, the P2 scribe was using a glass knife. Finally, 120 nm Ag contacts are thermally evaporated on the active area. The total active area of one module device was 7.26 cm^2 determined by the FTO pattern, P2 scribe, and Ag evaporation mask.

<u>Photovoltaic performance characterization:</u>

The current density-voltage (*J-V*) characteristics were measured with a Keithley 2400 Source Meter under AM 1.5G illumination using a Xenon-lamp solar simulator (XES-40S1, SAN-EI). Before the measurement, the light intensity of 100 mW cm^{-2} was calibrated using a standard monocrystalline silicon solar cell with a KG-5 filter. The active area of the device was defined with an aperture area of 0.07221 cm^2. The measurement conditions are as follows: Forward scan (−0.02 V to 1.26 V, scan rate 40 mV s^{-1}, and no delay time) and reverse scan (1.26 V to −0.02 V, scan rate 40 mV s^{-1}, and no delay time). The external quantum efficiency (EQE) spectrum was measured by a QE-R3011 measurement system (Enli Technology, Inc.). The steady-state power outputs (SPOs) of the non-encapsulated p-i-n PSC devices were measured at the maximum power point (MPP) under air-mass (AM) 1.5G solar illumination (100 mW cm^{-2}) in the air where the devices were cooled with the wind. The device was placed on top of the integrating globe, and only forward light emissions could be collected. The devices were swept from zero to forwarding bias with a 0.1 V step.

Stability assessment:

Thermal stability assessments for encapsulated devices were conducted by storing the encapsulated PSCs on a hot plate at 85℃ in an N_2 atmosphere. Photovoltaic performances were regularly measured when cooled down to room temperature. The encapsulation for the device was done by capping the device with a glass slide, using UV adhesive as the sealant. The encapsulation process was finished in an N_2-filled glovebox (with H_2O and O_2 concentrations of < 0.1 ppm). The long-term operational stability of the encapsulated devices was further assessed by tracking the SPO at MPP under full-spectrum white LED illumination (continuous 1-sun illumination) in ambient air (relative humidity ~30 ± 10 %), and the ambient temperature in the chamber was around 40℃ during device operation by electrical fans.

Film characterization:

Scanning electron microscope (SEM) (FEI Nova Nano SEM 430 & HITACHI U8010) was used to investigate the surface and cross-section morphology, with an accelerating voltage of 10 kV. The perovskite films were made by the same protocols used in solar cell fabrication. Grazing incidence wide-angle X-ray scattering (GIWAXS) measurements were conducted at Beijing Synchrotron Radiation Facility (BSRF). The wavelength of X-ray was 1.546 Å with the grazing incident angle of 0.7 degrees, and the scattering intensity was detected by an EIGER X 1M Detector Systems. DektakXT Stylus Profiler (Bruker) was used to measure thickness of perovskite films. Ultraviolet photoelectron spectroscopy (UPS) and X-ray photoelectron spectroscopy (XPS) measurements were performed using Thermofisher ESCALAB Xi^+ system. The apparatus was equipped with a monochromated Al target X-ray (1486.7 eV) and He UV light (22.12 eV) as the XPS and UPS excitation sources, respectively.

The magnetic immersion lens was carried out to enhance the collection of the photoelectron for XPS measurement. A bias of -10.0 V was applied between samples and the spectrometer for UPS measurement. The pass energy was set as 20.0 and 1.0 eV, and the scanning step was set at 0.05 eV per step and 0.02 eV per step for XPS high-resolution scan and UPS scan, respectively. An Ar ion raster size of 5 mm was applied to ensure the uniform region for XPS and UPS measurements. XPS and UPS spectra were recorded in the center of the sputtering spot. The data analysis was conducted by using the Avantage software package. The time-of-flight secondary ion mass spectrometry (ToF-SIMS) analysis was conducted using a PHI nano ToF II (ULVAC-PHI, Japan) system via the dual beam slice-and-view analysis scheme. All the ToF-SIMS results were obtained from a 50 μm × 50 μm area on the sample surface. The ejected secondary ions were accelerated by a sample bias of 3.0 kV, so the secondary ions could gain enough kinetic energy to reach the SIMS detector. All the secondary-ion data presented in the profiles were normalized by total ion intensities.

The samples for UV–vis absorption spectra characterization were prepared by spin-coating perovskite films on the ITO glass substrates. UV–vis absorption nature (350~850 nm) was then recorded with a spectrophotometer (UH4150, Hitachi, Japan). During the measuring process, the perovskite thin films were exposed to air for <5 min and the background noise was subtracted before testing. For the steady-state photoluminescence (PL) and time-resolved photoluminescence (TRPL) spectroscopy measurements, the samples were prepared on glasses. The preparation process of the control and target perovskite films preparation process was the same as that of the device fabrication. The steady-state PL and TRPL measurements were performed on an Edinburgh Instruments FLS1000 photoluminescence spectrometer (Edinburg, UK), and all TRPL-related tests were measured under the excitation wavelength of 450 nm after 150 s illumination. The surface roughness and potentials were measured by a commercial atom force microscopy (AFM, Cypher VRS, Oxford Instruments) in ambient conditions with the humidity of ~10%. The crystallographic structure was characterized by the X-ray diffraction (XRD) instrument (D8 Discover, Burker) using 40 kV, 40 mA radiation (Cu Kα, $\lambda = 0.15406$ nm). The Fourier transform infrared spectroscopy (FT-IR) analysis was performed using a Thermo Scientific Nicolet iS20 spectrometer. For nuclear magnetic resonance analysis, a Bruker 400MHz AVANCE III instrument was used to record ^{1}H-NMR spectra. 2-propanol-d8 was used as a solvent, with the signal from residual non-deuterated isopropanol solvent used to reference the spectra. In regard to ultrafast spectroscopy, the output of a Ti:sapphire amplifier system (Spectra Physics Solstice Ace) operating at 1 kHz and generating ~100 fs pulses was used to generated the pump pulses. The 400-nm pump pulses were created by sending the 800-nm fundamental beam through a second harmonic generating (SHG) beta barium borate (BBO) crystal (Eksma Optics). The broadband white probe was provided by the Disco (Leukos Laser, STM-2-UV) and the pump-probe decay was controlled electronically. The white light was split into two identical beams (probe and reference) by

a 50/50 beamsplitter. The reference beam passing through the sample did not interact with the pump, which allows for correcting for any shot-to-shot fluctuations in the probe that would otherwise greatly increase the structured noise in the experiments. Based on this arrangement, small signals with $\Delta T/T \sim 10^{-5}$ could be measured. The transmitted probe and reference pulses were collected with a silicon dual-line array detector (Hamamatsu S8381-1024Q, spectrograph: Andor Shamrock SR-303i-B) driven and read out by a custom-built board (Stresing Entwicklungsbüro).

Molecular Dynamics Simulation:

Molecular dynamics simulations were carried out using Materials Studio 2023. For the molecular model construction, Amorphous Cell Calculation was adopted; Forcite was used for calculation. In detail, simulations were carried out in NVT ensemble, 298 K, timestep of 1 fs, simulation duration of 1 ns, Velocity Scale thermostat, Universal force field were adopted. Ions are charged (iodide ions are negatively charged, others are positive), with output every 500 timesteps.

Supporting Figures and Tables

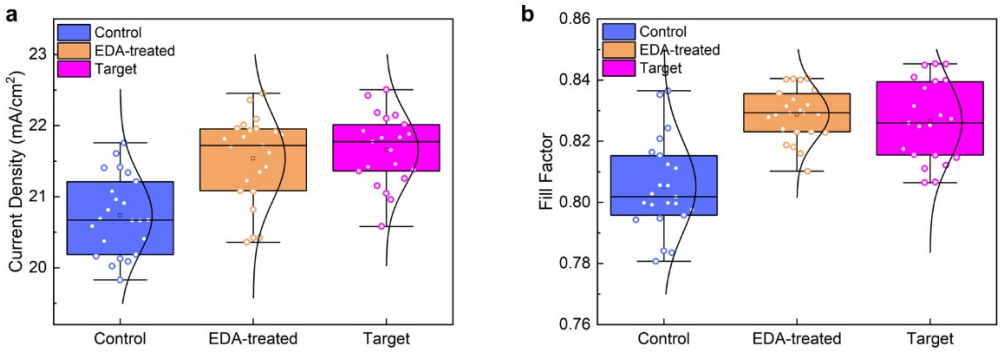

Figure S1. Statistical distributions of (a) Short-current density (J_{SC}) and (b) filling factor (FF) for control, EDA-treated, and target WBG PSCs.

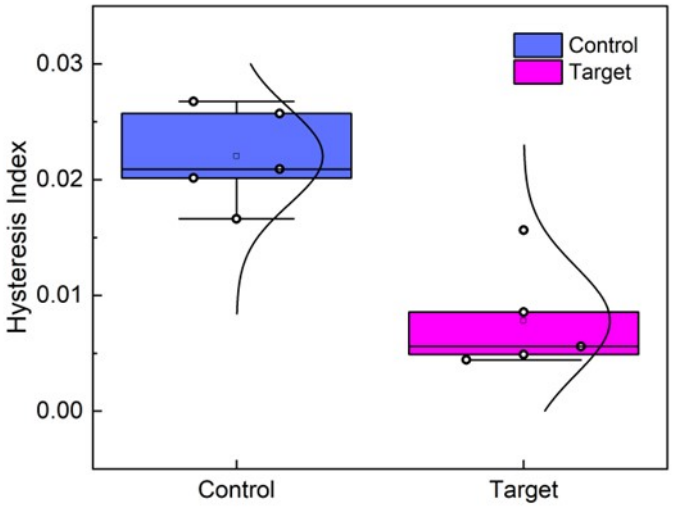

Figure S2. Five statistical distributions of hysteresis index for control, and target perovskite films.

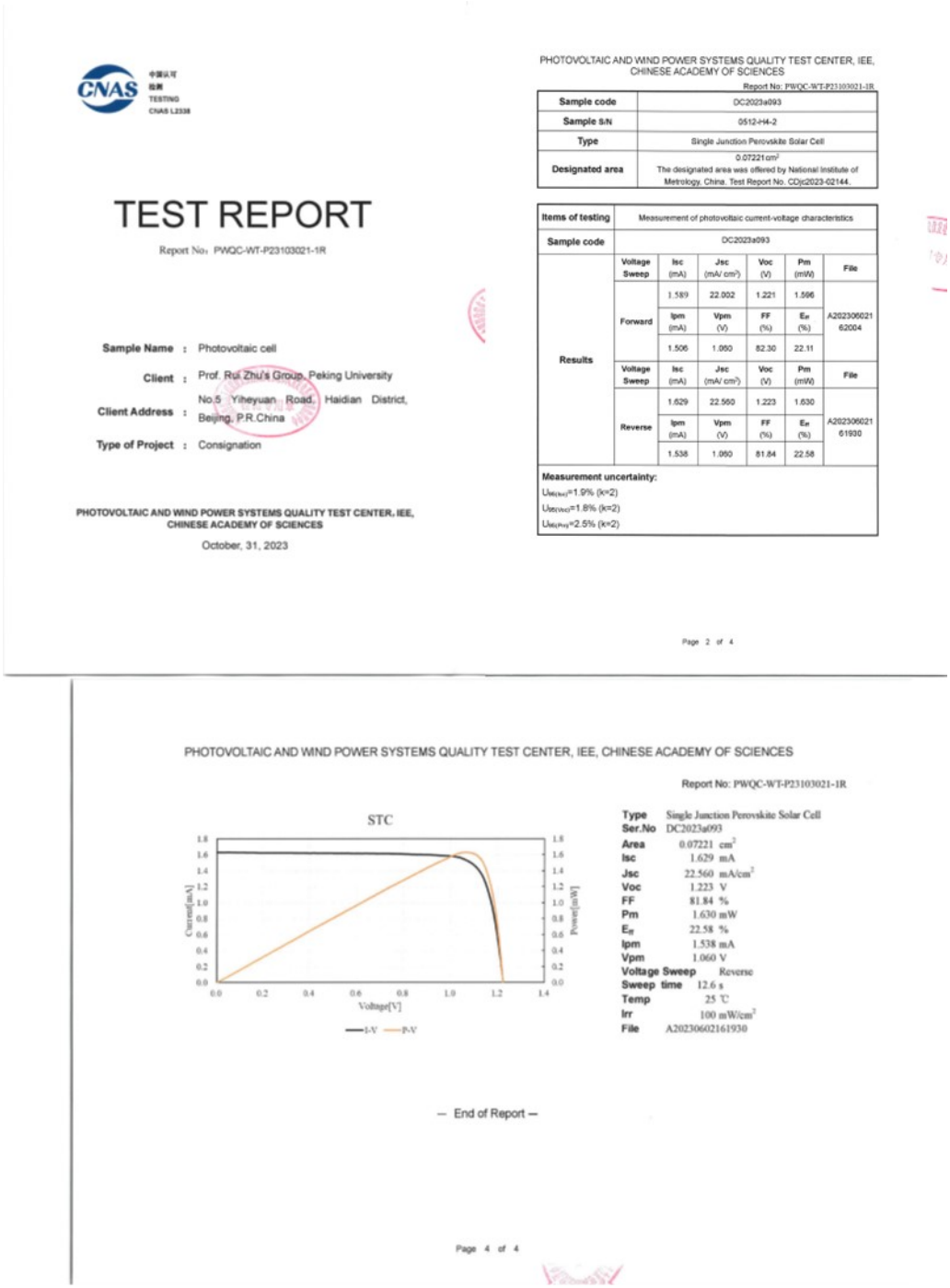

TEST REPORT

Report No：PWQC-WT-P23103021-1R

Sample Name ： Photovoltaic cell

Client ： Prof. Rui Zhu's Group, Peking University

Client Address ： No.5 Yiheyuan Road, Haidian District, Beijing, P.R.China

Type of Project ： Consignation

PHOTOVOLTAIC AND WIND POWER SYSTEMS QUALITY TEST CENTER, IEE, CHINESE ACADEMY OF SCIENCES

October, 31, 2023

PHOTOVOLTAIC AND WIND POWER SYSTEMS QUALITY TEST CENTER, IEE, CHINESE ACADEMY OF SCIENCES

Report No: PWQC-WT-P23103021-1R

Sample code	DC2023a093
Sample S/N	0512-H4-2
Type	Single Junction Perovskite Solar Cell
Designated area	0.07221 cm² The designated area was offered by National Institute of Metrology, China. Test Report No. CDjc2023-02144.

Items of testing	Measurement of photovoltaic current-voltage characteristics					
Sample code	DC2023a093					
Results	Voltage Sweep	Isc (mA)	Jsc (mA/ cm²)	Voc (V)	Pm (mW)	File
	Forward	1.589	22.002	1.221	1.596	A202306021 62004
		Ipm (mA)	Vpm (V)	FF (%)	E_ff (%)	
		1.506	1.060	82.30	22.11	
	Voltage Sweep	Isc (mA)	Jsc (mA/ cm²)	Voc (V)	Pm (mW)	File
	Reverse	1.629	22.560	1.223	1.630	A202306021 61930
		Ipm (mA)	Vpm (V)	FF (%)	E_ff (%)	
		1.538	1.060	81.84	22.58	

Measurement uncertainty:
$U_{rel(Isc)}$=1.9% (k=2)
$U_{rel(Voc)}$=1.8% (k=2)
$U_{rel(Pm)}$=2.5% (k=2)

Page 2 of 4

PHOTOVOLTAIC AND WIND POWER SYSTEMS QUALITY TEST CENTER, IEE, CHINESE ACADEMY OF SCIENCES

Report No: PWQC-WT-P23103021-1R

STC

Type	Single Junction Perovskite Solar Cell
Ser.No	DC2023a093
Area	0.07221 cm²
Isc	1.629 mA
Jsc	22.560 mA/cm²
Voc	1.223 V
FF	81.84 %
Pm	1.630 mW
E_ff	22.58 %
Ipm	1.538 mA
Vpm	1.060 V
Voltage Sweep	Reverse
Sweep time	12.6 s
Temp	25 ℃
Irr	100 mW/cm²
File	A202306021619 30

— End of Report —

Page 4 of 4

Figure S3. Certification report for small area WBG PSCs. The report is issued by PWQC (PHOTOVOLTAIC AND WIND POWER SYSTEMS QUALITY TEST CENTER, IEE, CHINESE ACADEMY OF SCIENCES).

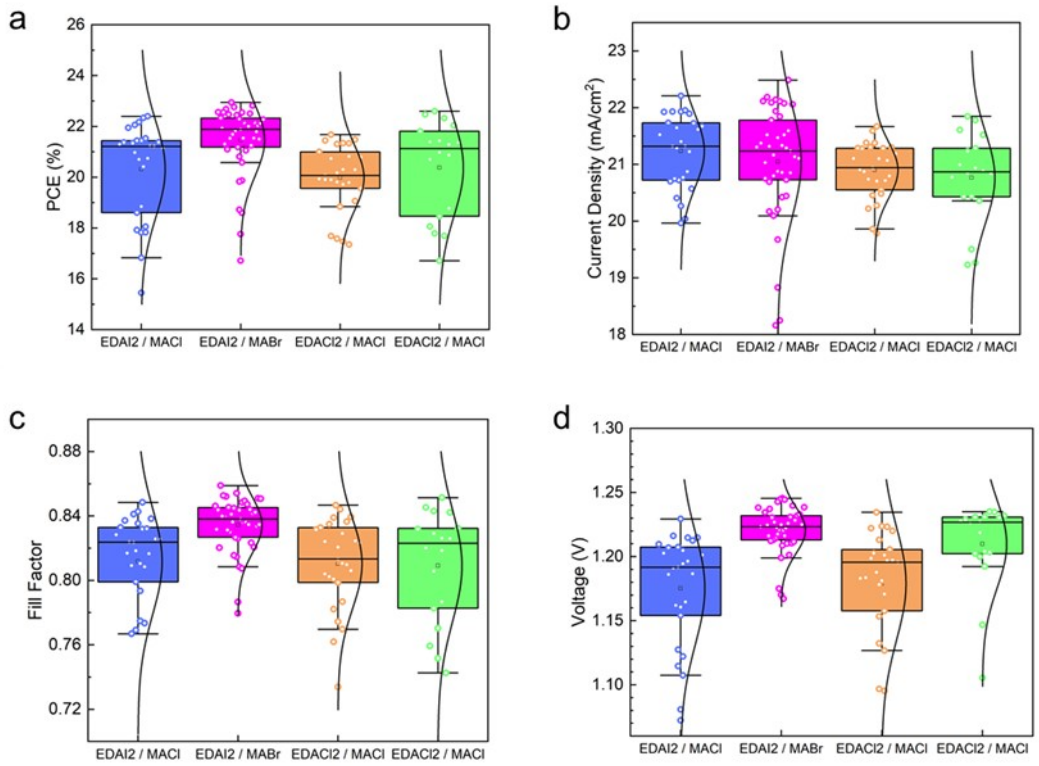

Figure S4. Statistical distributions of (a) PCE, (b) J_{SC}, (c) fill factor and (d) V_{OC} for different post-treatment combination WBG PSCs.

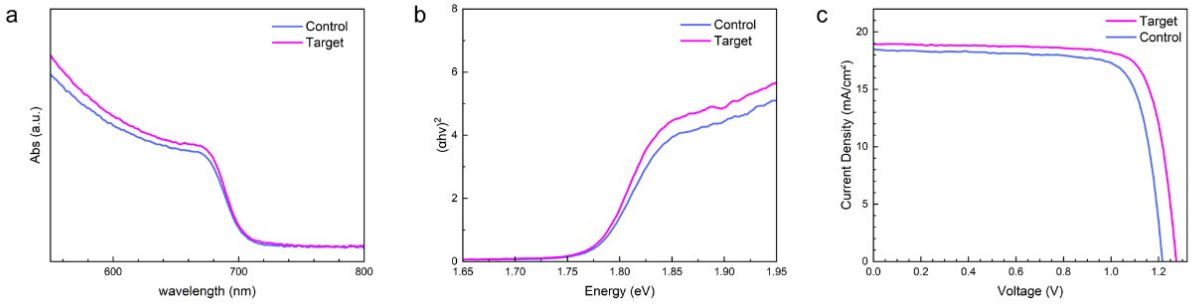

Figure S5. (a) UV-visible absorption spectroscopy of the control and target 1.77-eV perovskite films. (b) A 1.77-eV bandgap of the perovskite films was determined via the Tauc plot. (c) The best current density-voltage (*J-V*) curves of control and target 1.77-eV PSCs.

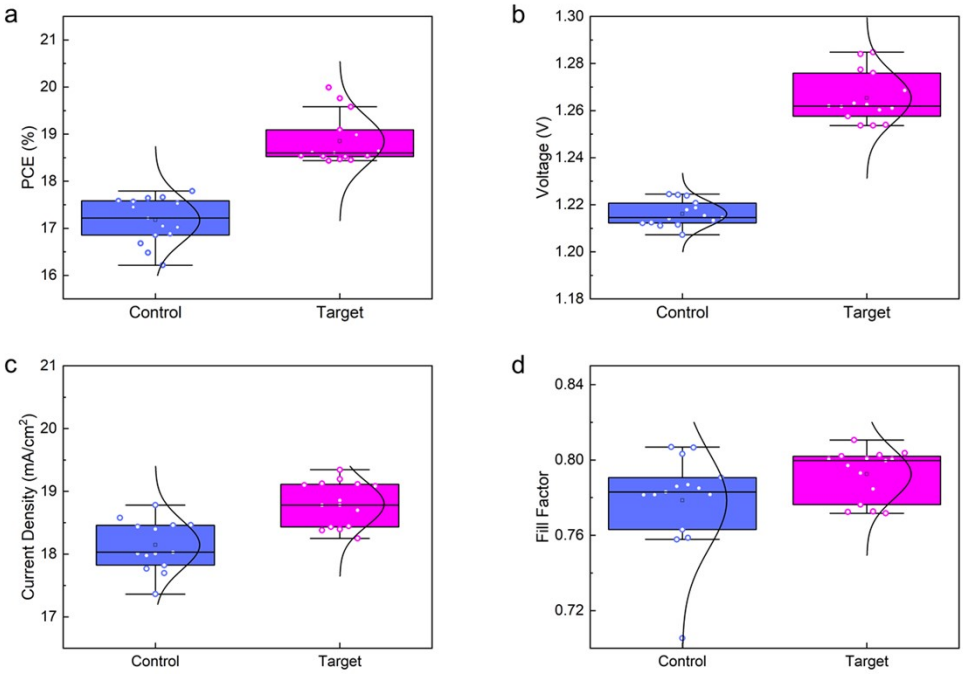

Figure S6. Statistical distributions of (a) PCE, (b) V_{OC}, (c) J_{SC} and (d) fill factor for control and target 1.77-eV PSCs.

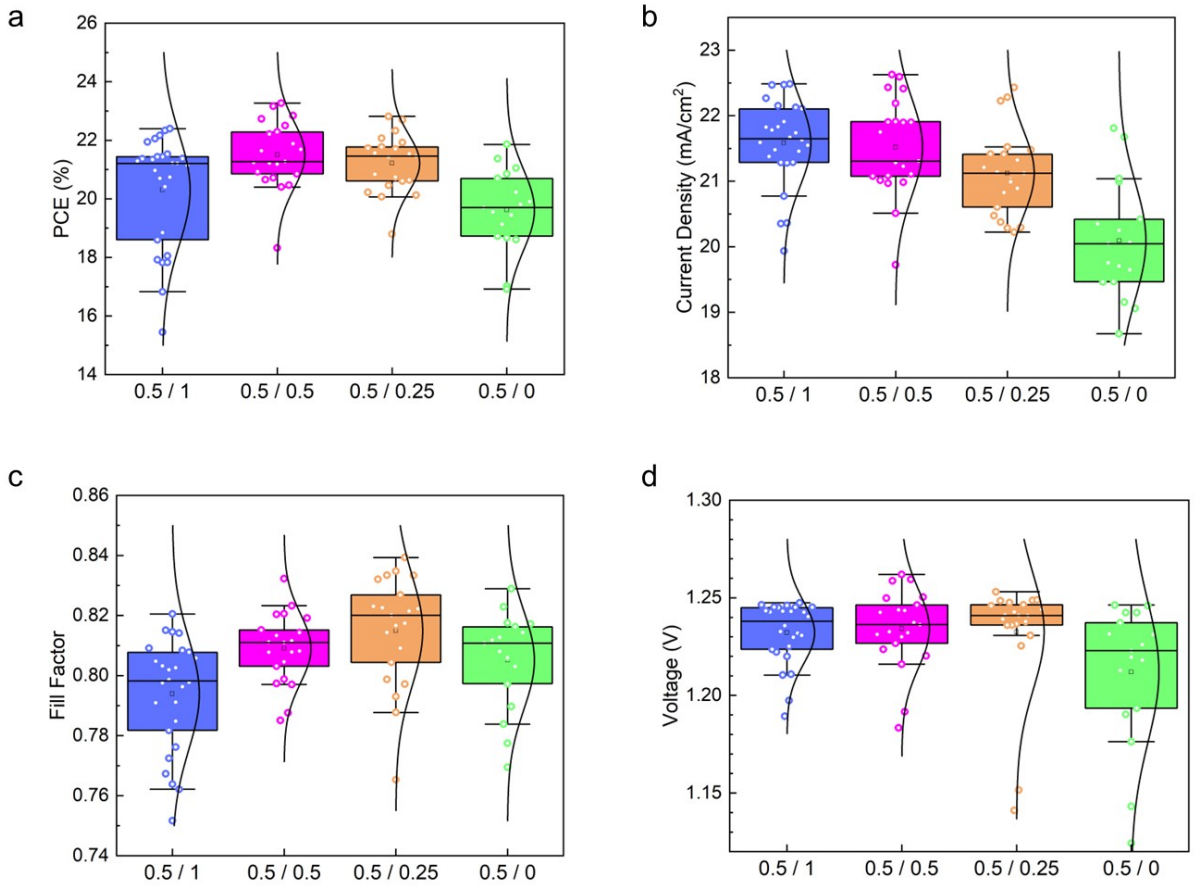

Figure S7. Statistical distributions of (a) PCE, (b) J_{SC}, (c) fill factor and (d) V_{OC} for post-treatment ratio $EDABr_2$: MAI = 0.5/0 0.5/0.25 0.5/0.5 0.5/1.0 (concentration unit: mg/ml) WBG PSCs.

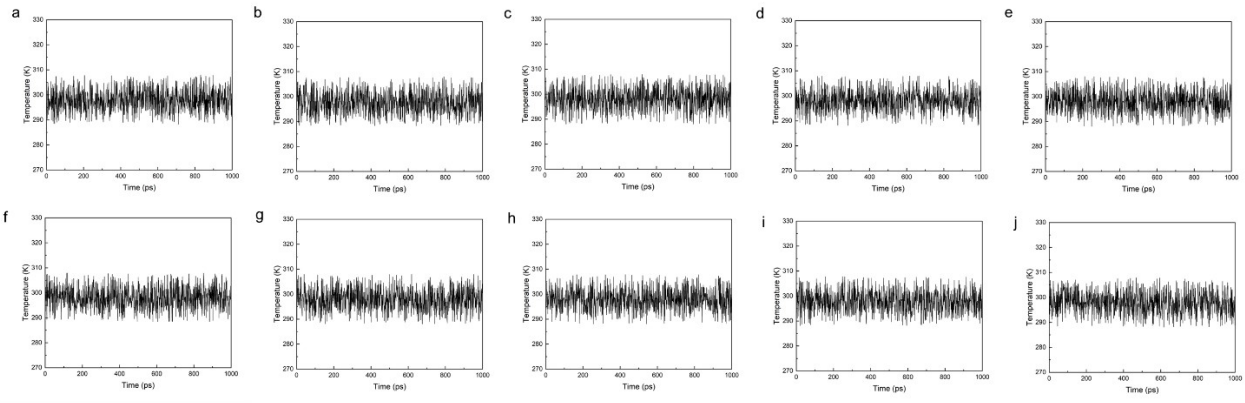

Figure S8. Temperature over time plot of 10 independent molecular dynamics simulations. (a)~(e) are EDA-FA. (f)~(j) are EDA-FA-MA.

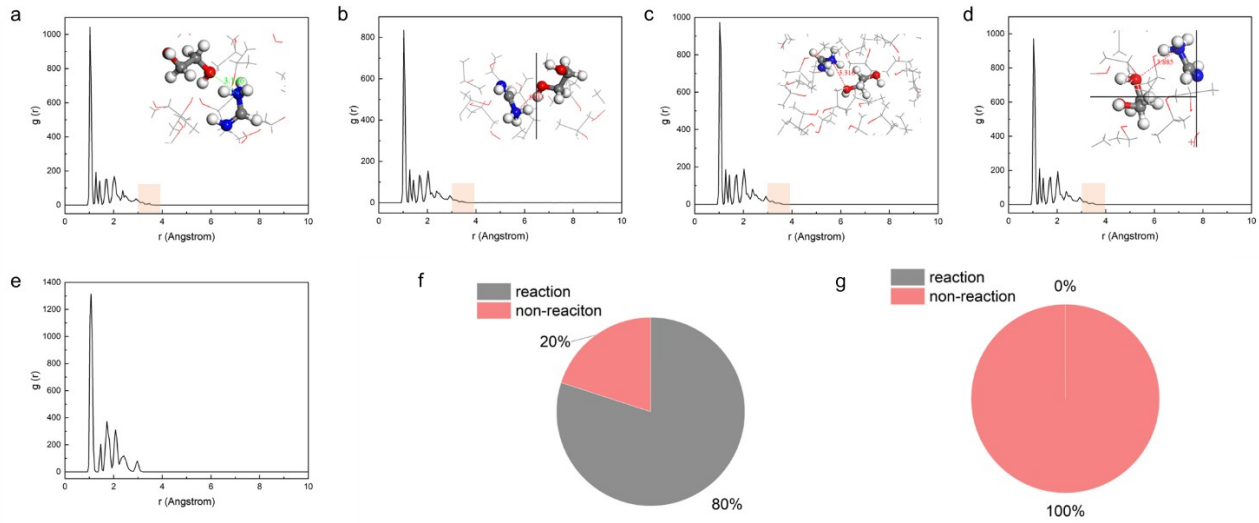

Figure S9. (a)~(d) The radial distribution function (RDF) of 4 individual EDA-FA reaction. The inset shows the representative EDA-FA interaction configuration. (e) Representative RDF of a simulation without EDA-FA interaction. (f)~(g) are probability distribution pie charts derived from five simulations each for the EDA+FA and EDA+FA+MA systems, respectively.

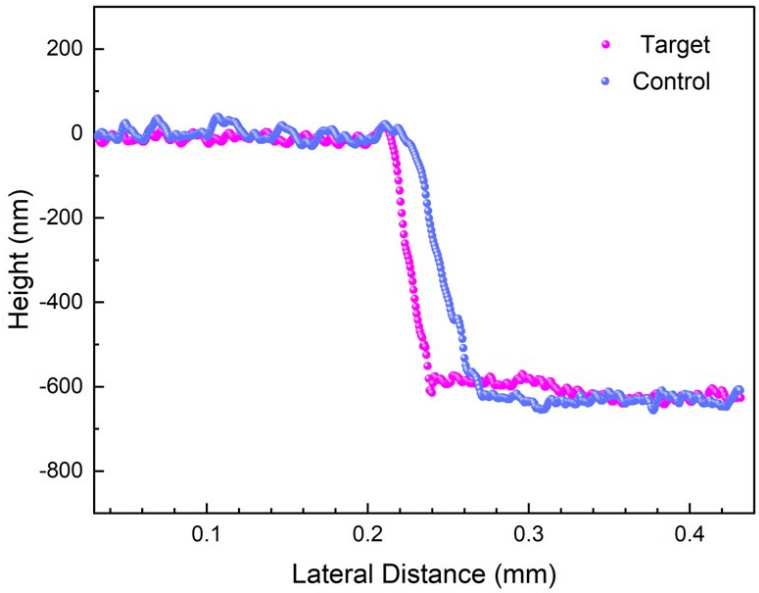

Figure S10. Stylus profiler of the control and target perovskite films.

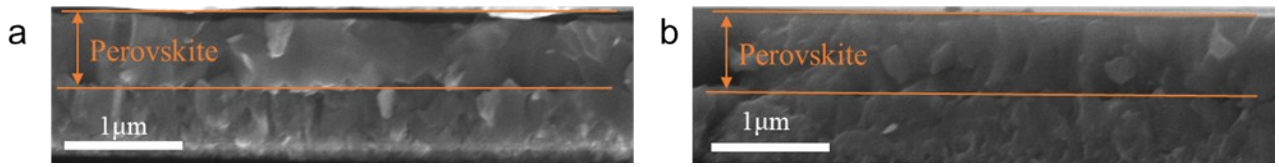

Figure S11. Cross-section SEM image of control (a) and target (b) perovskite films.

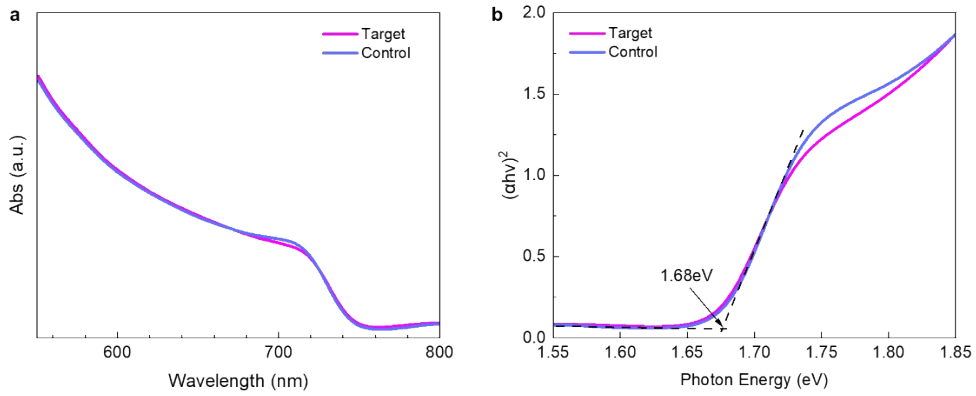

Figure S12. (a) UV-visible (UV-vis) absorption spectroscopy of the control and target perovskite films. (b) A 1.68-eV bandgap of the perovskite films was determined via the Tauc plot.

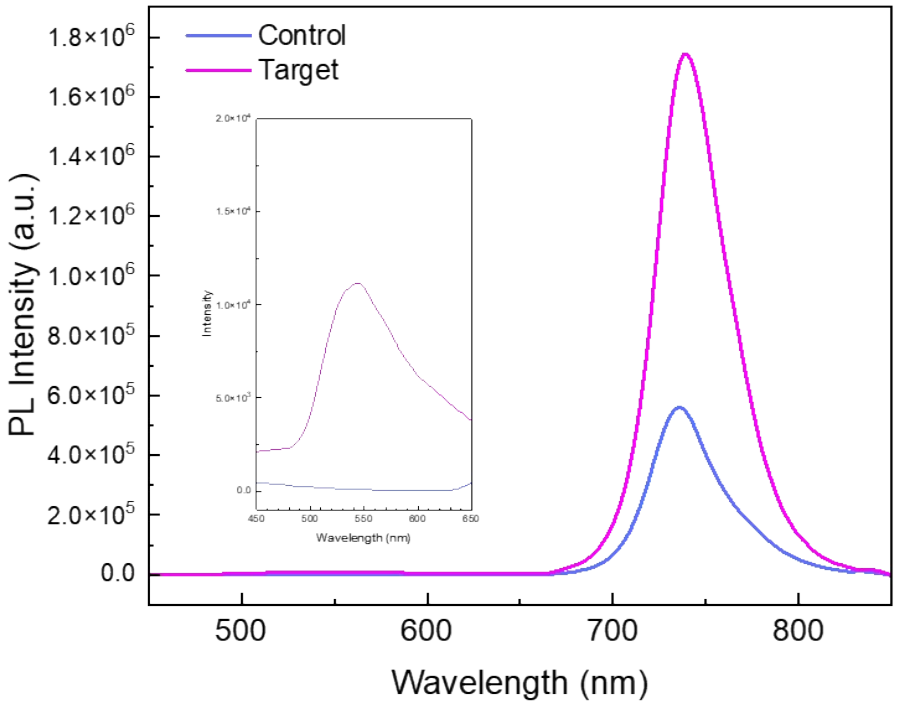

Figure S13. Steady-state photoluminescence (PL) spectra of control and target perovskite films. The inset shows 2D perovskite peak in ~540nm.

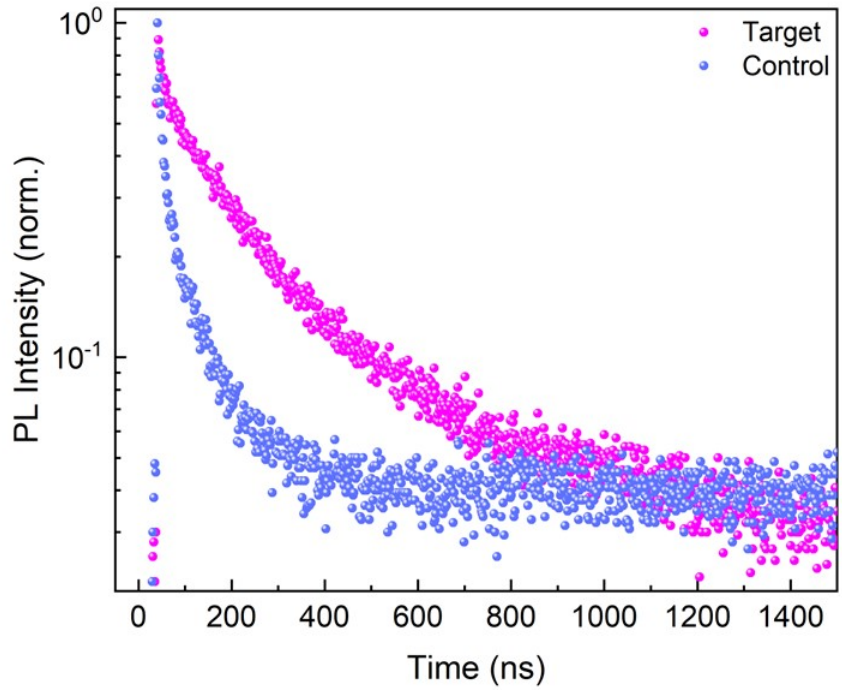

Figure S14. Time-resolved photoluminescence (TRPL) spectra of control and target perovskite films.

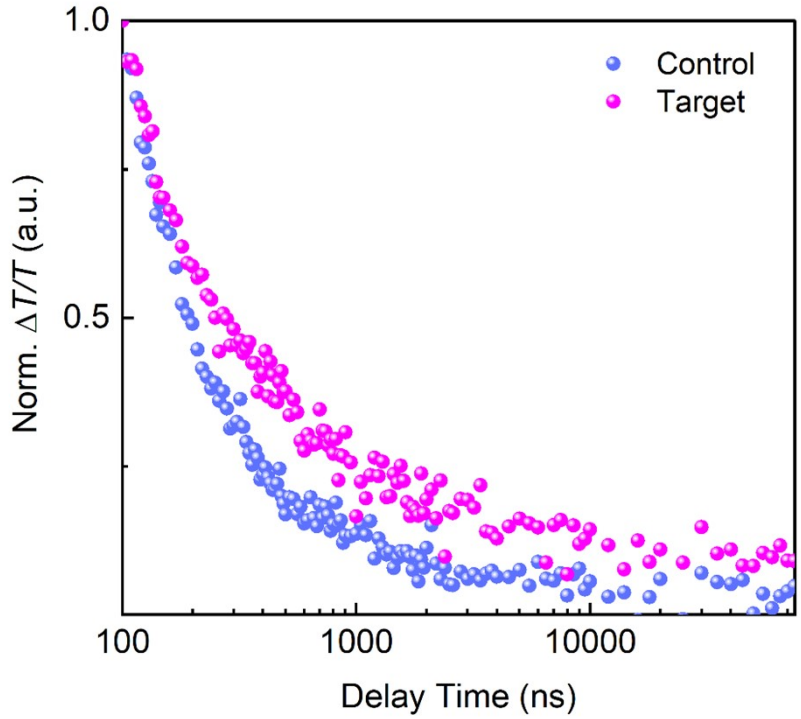

Figure S15. Normalized ultrafast spectroscopy kinetics at the GSB of 3D perovskite. The decay is

normalized to 100 ns after excitation. Samples were photoexcited at 400 nm at the repetition rate of 1 kHz. The fluence of the laser is around 12.24 μJ cm^{-2}.

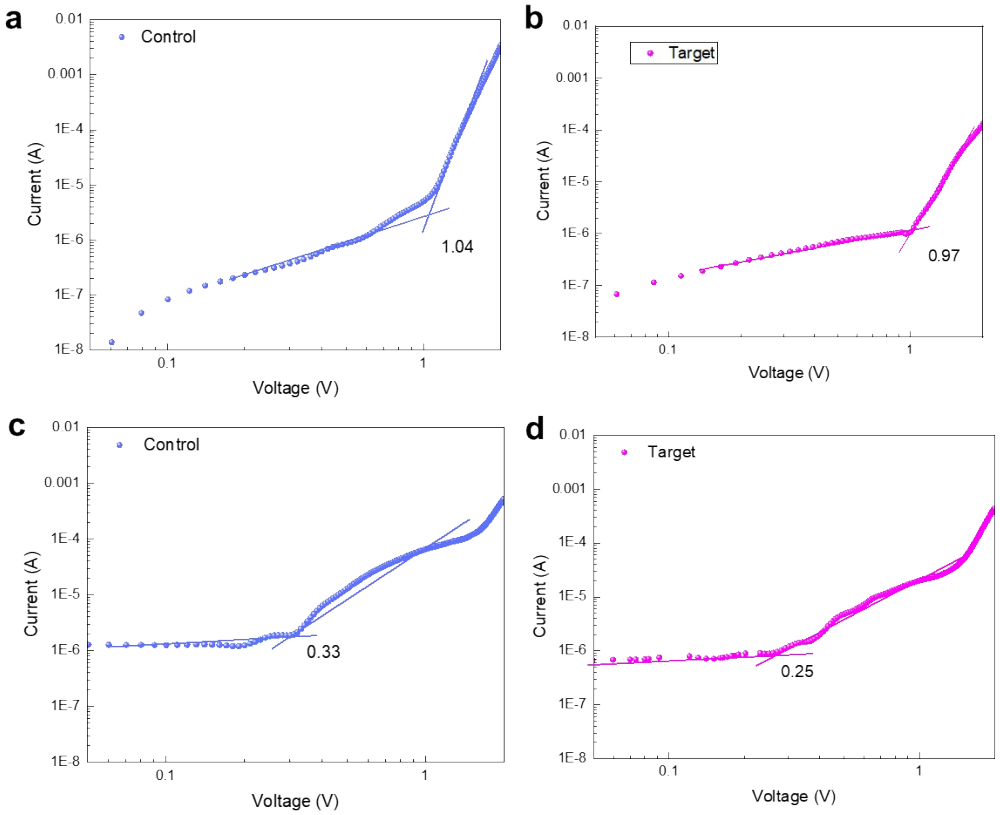

Figure S16. Dark *J-V* curves of hole-only devices (a) control, (b) target; Dark *J-V* curves of electron-only devices (c) control, (d) target.

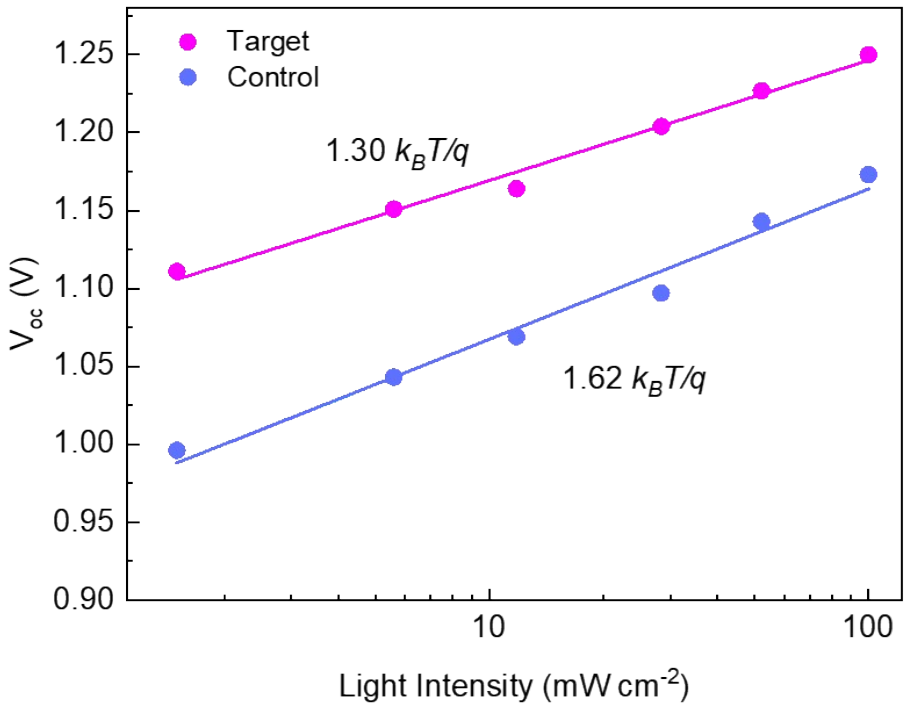

Figure S17. Linear relationship between V_{OC} and the incident light intensity.

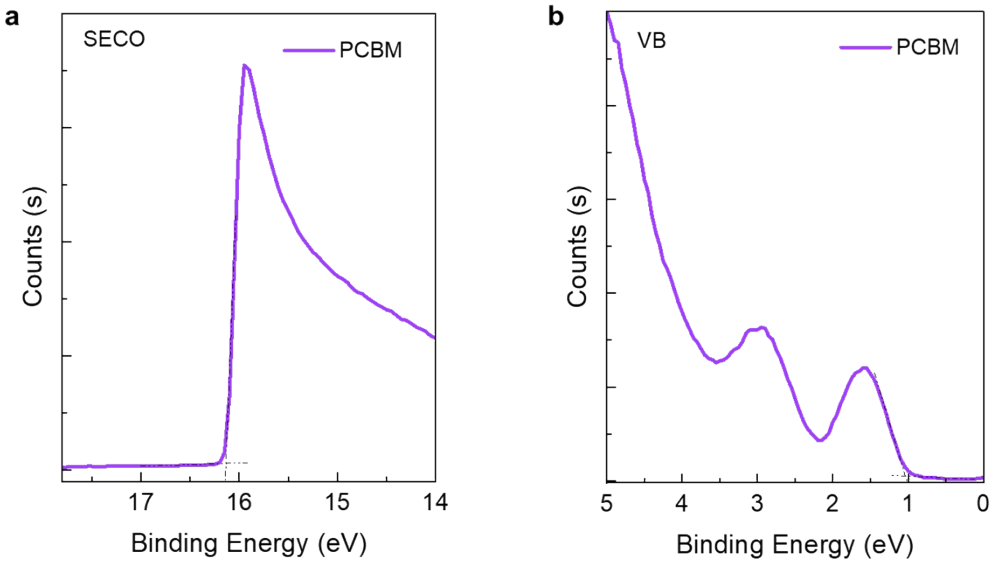

Figure S18. SECO (a) and VB (b) of PCBM film.

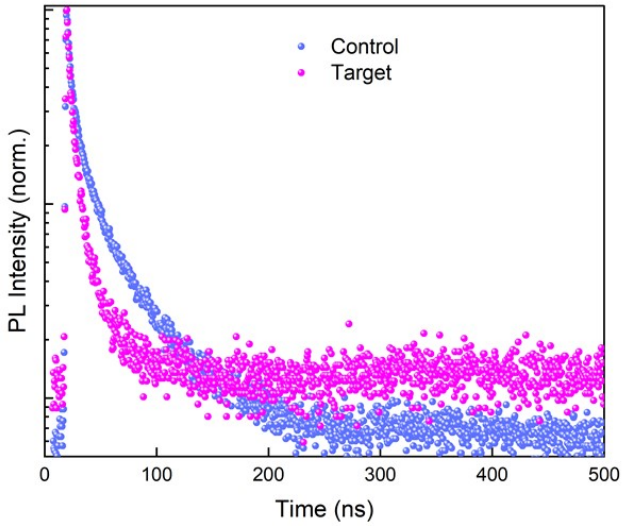

Figure S19. TRPL spectra of control and target perovskite films (sample structure: glass/Perovskite/$PC_{61}BM$).

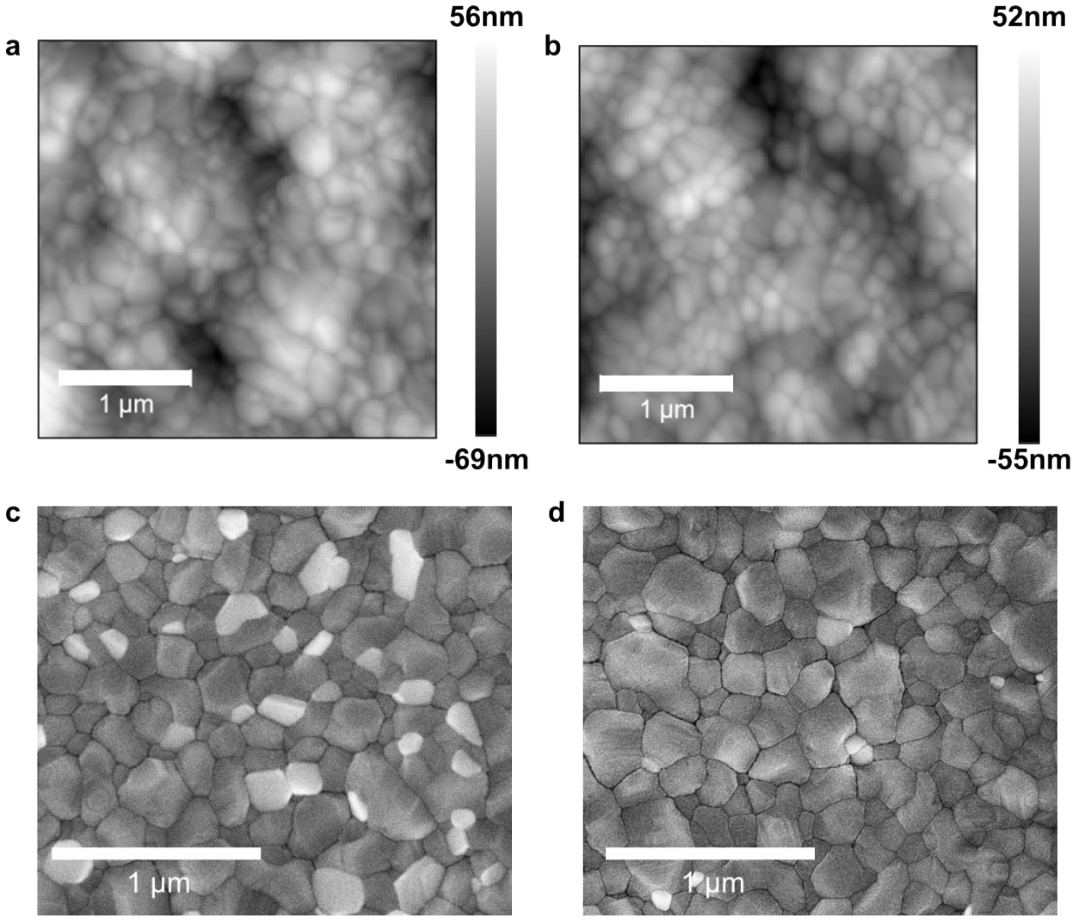

Figure S20. Top-view atomic force microscopy (AFM) images of the control (a) and target (b)

perovskite films. Scanning electron microscopy (SEM) images of the control (c) and target (d) perovskite films top surface.

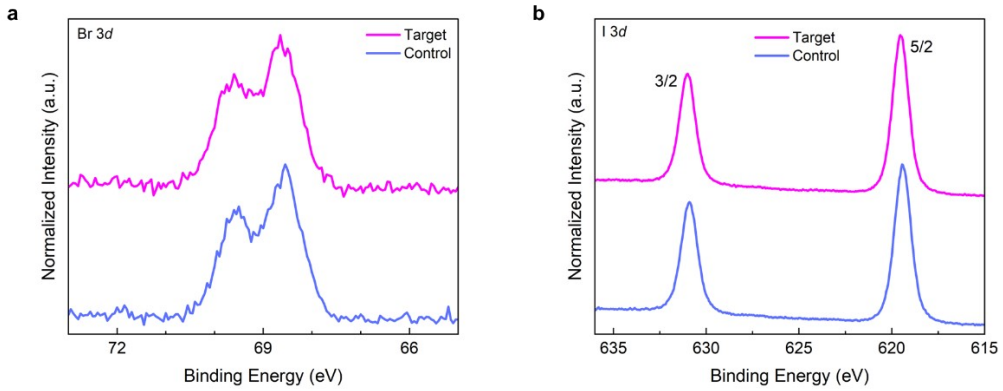

Figure S21. XPS spectra of element Br (a) and element I (b) of control and target perovskite films.

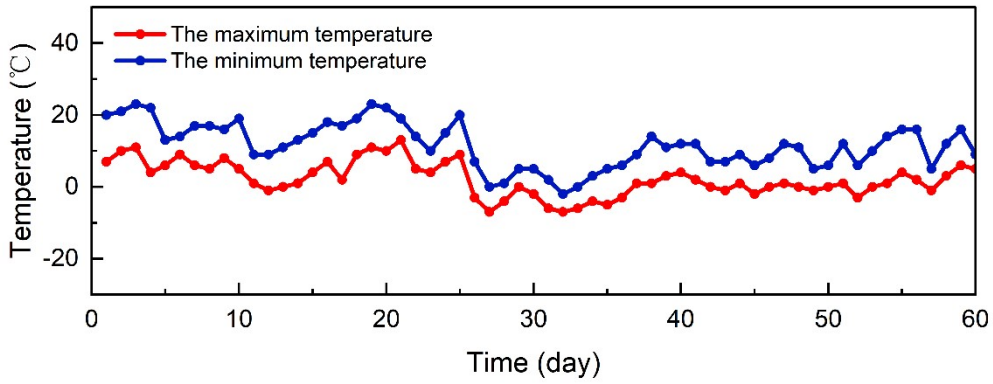

Figure S22. Line chart of temperature change for encapsulated mini-module outdoor stability test.

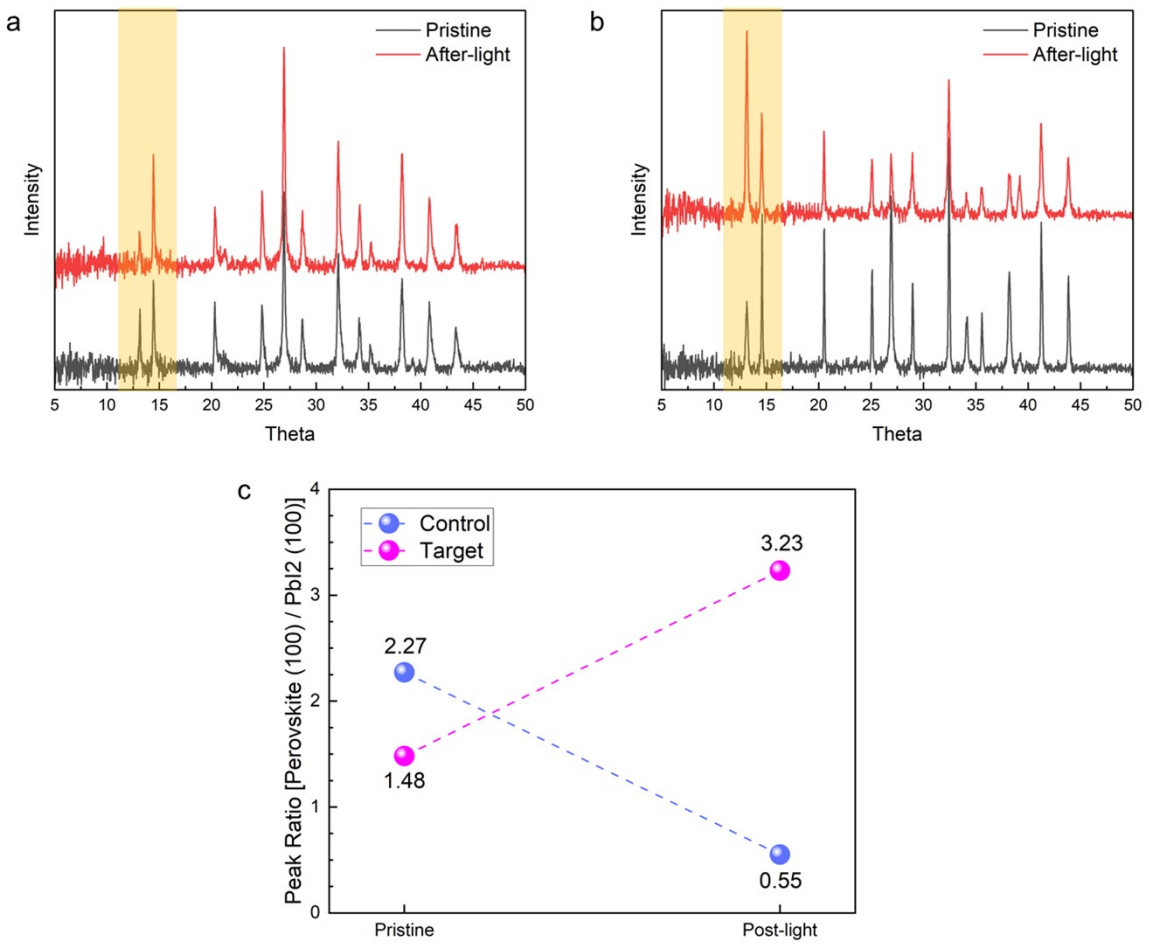

Figure S23. X-Ray diffraction pattern of fresh and post-degradation perovskite films for (a) with and (b) without dual-ammonium treatment. (c) Peak ratios of perovskite (100) facet to PbI_2 (100) facet of pristine and post-light sample.

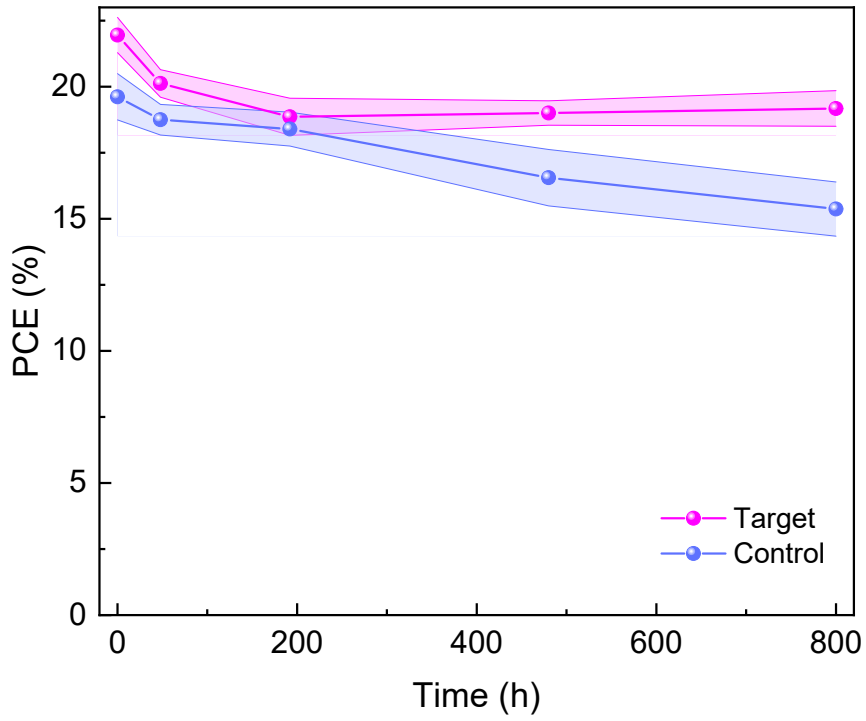

Figure S24. Long-term stability of small area (~0.1 cm^2) devices stored in N_2 glovebox at 85°C.

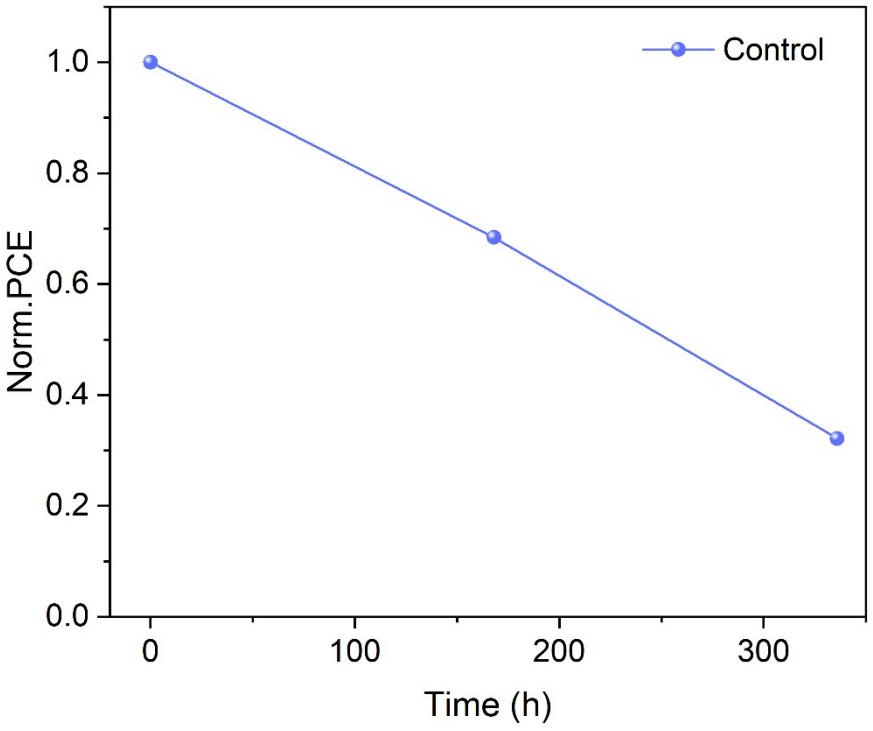

Figure S25. Outdoor performance of the encapsulated control modules

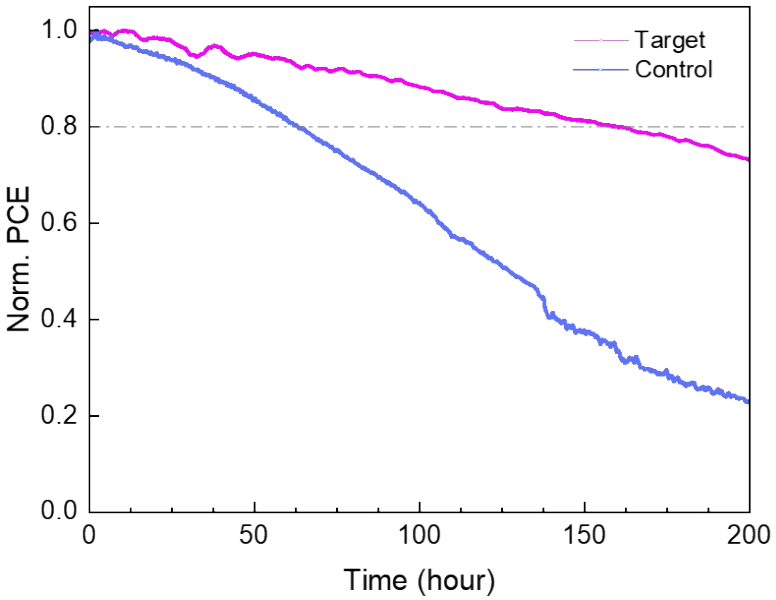

Figure S26. The maximum power point (MPP) tracking of the encapsulated control and target devices.

Table S1. Photovoltaic performance metrics of state-of-the-art WBG (1.65~1.70 eV) PSCs related to **Figure 1**.

Published time (year/month)	E_g (eV)	V_{OC} (V)	FF (%)	PCE (%)	Reference
2022/03	1.68	1.20	81.7	20.39	[1]
2022/05	1.65	1.21	80.5	20.53	[2]
2022/07	1.68	1.21	79.5	20.11	[3]
2022/07	1.65	1.23	83.8	21.9	[4]
2023/01	1.68	1.22	80.3	22.3	[5]
2023/03	1.67	1.25	81.0	20.06	[6]
2023/05	1.65	1.26	79.4	21.8	[7]
2023/07	1.70	1.26	81.6	22.19	[8]
2023/07	1.68	1.28	78.8	20.58	[9]
2023/08	1.68	1.16	81.0	21.44	[10]
This work	1.68	1.25	83.1	23.05	

Table S2. Photovoltaic parameters of devices in **Figure 1**.

Active area	V_{OC} (V)	J_{SC} (mA cm^{-2})	FF	PCE (%)	Notes
0.10 cm^2	1.25	22.31	0.83	23.05%	
1.00 cm^2	1.24	21.33	0.80	21.25%	
7.26 cm^2 (Mini-module)	7.18	25.5mA	0.79	20.1%	The J_{SC} column shows electric current

Table S3. Stylus profiler raw data of 5 samples for control and target group.

Sample No.	No.1 (nm)	No.2 (nm)	No.3 (nm)	No.4 (nm)	No.5 (nm)	Average Height (nm)
Control	631	642	640	644	638	639
Target	639	635	644	641	646	641

Table S4. The decay curves of TRPL results are fitted according to the formula: $y = A_1e^{-x1/\tau1} + A_2e^{-x2/\tau2} + B$. Carrier lifetimes are calculated by the formula: $\tau_{ave} = \sum A_i\tau_i^2/A_i\tau_i$.

Sample	τ_1 (ns)	τ_2 (ns)	A_1	A_2	τ_{ave} (ns)	R^2
Control	7.40 ± 0.14	74.72 ± 1.11	0.69 ± 0.01	0.31 ± 0.01	62.57±1.29	0.991
Target	11.32 ± 0.46	201.75± 1.55	0.39± 0.01	0.61± 0.01	195.16±1.49	0.993
Control with $PC_{61}BM$	3.01 ± 0.03	25.78 ± 0.24	0.71 ± 0.01	0.29 ± 0.01	20.75±0.20	0.997
Target with $PC_{61}BM$	2.43 ± 0.03	10.92 ± 0.18	0.70± 0.01	0.30± 0.01	7.99±0.14	0.997

Table S5. The ultrafast spectroscopy measurement curves are fitted according to the formula: $y = A_1e^{-x1/t_1} + B$. Monomolecular non-radiative recombination coefficients are calculated by the

formula: $k_1 = {}^1/_{t_1}$.[11]

Sample	A_1	t_1 (ns)	k_1 (s^{-1})	R^2
Control	1.44±0.05	170.66±6.69	(5.85±0.20)×10^6	0.963
Target	0.92±0.03	311.28±16.31	(3.21±0.17)×10^6	0.940

Table S6. The statistical result of weather for encapsulated mini-module outdoor stability test.

Weather	Clear	Overcast	Rainy	Snowy
Number of days	24	26	9	1

Note S1. The hysteresis index (HI) or hysteresis factor can be can be calculated through the following formula:

$$Hysteresis\ Index\ (HI) = \frac{\int_{SC}^{OC} (J_{RS}(V) - J_{FS}(V))dV}{\int_{SC}^{OC} J_{RS}(V)dV}$$

Where the J is the current density, V is the applied voltage, SC is the short circuit, OC is the open circuit, RS is the reverse scan and FS is the forward scan. Solar cells with significant J-V hysteresis tend to have a high HI. Conversely, solar cells with a low HI exhibit minimal hysteresis effect during forward and reverse scans.[12]

Note S2. Space charge limited current method applied to the electron- or hole-only devices is employed to study the trap densities in semiconductors. As the bias voltage increases, two characteristic regions can be recognized: ohmic region and trap-filled region. When in the low bias voltage, the current increases linearly with the bias voltage (the ohmic region). As the bias voltage increases, the electron- or hole-traps will be filled by the injecting carriers, resulting in a sharp increase of the current (the trap-filled region). Thus, the electron or hole trap densities can be defined as,[13]

$$N_{trap} = \frac{2\varepsilon\varepsilon_0 V_{TFL}}{eL^2}$$

where N_{trap} is the defect density, ε and ε_0 are the static permittivity of perovskite and permittivity of free space, e is the elementary charge, and L is the thickness of the perovskite film.

Note S3. <u>The V_{OC}-light intensity dependence test</u>

The semilogarithmic of the V_{OC}-light intensity curve is taken, and the ideal factor (n) can be calculated by extracting the slope of the curve in the dominant region of diffusion current through the following formula:

$$n = \frac{q \quad dV_{oc}}{k_B T d(\ln L)}$$

where q is the elementary charge, k_B is the Boltzmann constant, L is the light intensity, and T is temperature. The light intensity dependence of V_{OC} in **Figure S8** shows that the control devices exhibit a strong dependence of V_{OC} on the light intensity, with a slope of 1.62 k_BT/q. The lower slope of 1.30 k_BT/q for the target device indicates suppressed trap assisted recombination under open-circuit conditions due to the reduced trap density in the heterostructure perovskite film.

Reference

1. Z. M. Fang, L. B. Jia, N. Yan, X. F. Jiang, X. D. Ren, S. F. Yang and S. Z. Liu, *Infomat*, 2022, **4**, e12307.
2. L. N. Wang, Q. Z. Song, F. T. Pei, Y. H. Chen, J. Dou, H. Wang, C. B. Shi, X. Zhang, R. D. Fan, W. T. Zhou, Z. W. Qiu, J. Q. Kang, X. Y. Wang, A. Lambertz, M. R. Sun, X. X. Niu, Y. Ma, C. Zhu, H. P. Zhou, J. W. Hong, Y. Bai, W. Y. Duan, K. N. Ding and Q. Chen, *Advanced Materials*, 2022, **34**, 2201315.
3. Y. T. Zheng, X. Y. Wu, J. H. Liang, Z. F. Zhang, J. K. Jiang, J. L. Wang, Y. Huang, C. C. Tian, L. Y. Wang, Z. H. Chen and C. C. Chen, *Advanced Functional Materials*, 2022, **32**, 2200431.
4. G. Yang, Z. Y. Ni, Z. S. Yu, B. W. Larson, Z. H. Yu, B. Chen, A. Alasfour, X. Xiao, J. M. Luther, Z. C. Holman and J. S. Huang, *Nature Photonics*, 2022, **16**, 588-594.
5. P. J. Hang, C. X. Kan, B. Li, Y. X. Yao, Z. C. Hu, Y. Q. Zhang, J. S. Xie, Y. Wang, D. R. Yang and X. G. Yu, *Advanced Functional Materials*, 2023, **33**, 2214381.
6. X. P. Zhang, X. Y. Li, L. Tao, Z. M. Zhang, H. Ling, X. Fu, S. B. Wang, M. J. Ko, J. S. Luo, J. Z. Chen and Y. L. Li, *Small*, 2023, **19**, 2208289.
7. Z. X. Li, X. Li, X. G. Chen, X. X. Cui, C. L. Guo, X. Z. Feng, D. X. Ren, Y. Q. Mo, M. Yang, H. W. Huang, R. Jia, X. P. Liu, L. Y. Han, S. Y. Dai and M. L. Cai, *Joule*, 2023, **7**, 1363-1381.
8. Z. L. Song, J. Yang, X. Y. Dong, R. Wang, Y. X. Dong, D. X. Liu and Y. S. Liu, *Nano letters*, 2023, **23**, 6705-6712.
9. S. Mariotti, E. Köhnen, F. Scheler, K. Sveinbjörnsson, L. Zimmermann, M. Piot, F. J. Yang, B. R. Li, J. Warby, A. Musiienko, D. Menzel, F. L. Lang, S. Kessler, I. Levine, D. Mantione, A. Al-Ashouri, M. S. Härtel, K. Xu, A. Cruz, J. Kurpiers, P. Wagner, H. Köbler, J. Z. Li, A. Magomedov, D. Mecerreyes, E. Unger, A. Abate, M. Stolterfoht, B. Stannowski, R. Schlatmann, L. Korte and S. Albrecht, *Science*, 2023, **381**, 63-69.
10. X. Niu, N. Li, Z. Cui, L. Li, F. Pei, Y. Lan, Q. Song, Y. Du, J. Dou, Z. Bao, L. Wang, H. Liu, K. Li, X. Zhang, Z. Huang, L. Wang, W. Zhou, G. Yuan, Y. Chen, H. Zhou, C. Zhu, G. Liu, Y. Bai and Q. Chen, *Advanced Materials*, 2023, **35**, 2305822.
11. L. Dai, Z. Deng, F. Auras, H. Goodwin, Z. Zhang, J. C. Walmsley, P. D. Bristowe, F. Deschler and N. C. Greenham, *Nature Photonics*, 2021, **15**, 696-702.
12. D.-H. Kang and N.-G. Park, *Advanced Materials*, 2019, **31**, 1805214.
13. Y. Zheng, X. Yang, R. Su, P. Wu, Q. Gong and R. Zhu, *Advanced Functional Materials*, 2020, **30**, 2000457.